The Astrophysical Journal Letters, 778:L24 (7pp), 2013 December 1 doi:10.1088/2041-8205/778/2/L24

EXPLORING THE CHEMICAL LINK BETWEEN LOCAL ELLIPTICALS AND THEIR HIGH-REDSHIFT PROGENITORS

Joel Leja[1], Pieter G. van Dokkum[1], Ivelina Momcheva[1], Gabriel Brammer[2], Rosalind E. Skelton[3], Katherine E. Whitaker[4], Brett H. Andrews[5], Marijn Franx[6], Mariska Kriek[7], Arjen van der Wel[8], Rachel Bezanson[9], Charlie Conroy[10], Natascha Förster Schreiber[11], Erica Nelson[1], and Shannon G. Patel[6]

[1] Department of Astronomy, Yale University, New Haven, CT 06511, USA
[2] European Southern Observatory, Alonson de Córdova 3107, Casilla 19001, Vitacura, Santiago, Chile
[3] South African Astronomical Observatory, Observatory Road, Cape Town, South Africa
[4] Astrophysics Science Division, Goddard Space Center, Greenbelt, MD 20771, USA
[5] Department of Astronomy, The Ohio State University, Columbus, OH 43210, USA
[6] Leiden Observatory, Leiden University, P.O. Box 9513, NL 2300 RA, Leiden, The Netherlands
[7] Astronomy Department, University of California at Berkeley, Berkeley, CA 94720, USA
[8] Max-Planck Institute for Astronomy (MPIA), Königstuhl 17, D-69117 Heidelberg, Germany
[9] Steward Observatory, University of Arizona, 933 North Cherry Avenue, Tucson, AZ 85721, USA
[10] Department of Astronomy & Astrophysics, University of California, Santa Cruz, CA, USA
[11] Max-Planck-Institut für extraterrestrische Physik, Giessenbachstrasse, D-85748 Garching, Germany
Received 2013 September 16; accepted 2013 October 23; published 2013 November 8

ABSTRACT

We present Keck/MOSFIRE *K*-band spectroscopy of the first mass-selected sample of galaxies at $z \sim 2.3$. Targets are selected from the 3D-*Hubble Space Telescope* Treasury survey. The six detected galaxies have a mean [N II]λ6584/Hα ratio of 0.27 ± 0.01, with a small standard deviation of 0.05. This mean value is similar to that of UV-selected galaxies of the same mass. The mean gas-phase oxygen abundance inferred from the [N II]/Hα ratios depends on the calibration method, and ranges from $12+\log(\mathrm{O/H})_{\mathrm{gas}} = 8.57$ for the Pettini & Pagel calibration to $12+\log(\mathrm{O/H})_{\mathrm{gas}} = 8.87$ for the Maiolino et al. calibration. Measurements of the stellar oxygen abundance in nearby quiescent galaxies with the same number density indicate $12+\log(\mathrm{O/H})_{\mathrm{stars}} = 8.95$, similar to the gas-phase abundances of the $z \sim 2.3$ galaxies if the Maiolino et al. calibration is used. This suggests that these high-redshift star forming galaxies may be progenitors of today's massive early-type galaxies. The main uncertainties are the absolute calibration of the gas-phase oxygen abundance and the incompleteness of the $z \sim 2.3$ sample: the galaxies with detected Hα tend to be larger and have higher star formation rates than the galaxies without detected Hα, and we may still be missing the most dust-obscured progenitors.

Key words: galaxies: abundances – galaxies: evolution

Online-only material: color figures

1. INTRODUCTION

Observations of the elemental abundances of galaxies provide information on the build-up of metals in the Universe and on the importance of winds and feedback (Davé et al. 2012). Most studies find that the mass–metallicity relation evolves with redshift, such that at fixed stellar mass, galaxies have lower metallicity at earlier times (Erb et al. 2006b; Maiolino et al. 2008; Zahid et al. 2013; though see also Stott et al. 2013). This is consistent with expectations from simple models in which gas is gradually enriched by (post-)asymptotic giant branch stars and supernovae.

In addition to measuring their gas-phase metallicities, it is also possible to measure the *stellar* metallicities of galaxies (Gallazzi et al. 2005; Panter et al. 2008; Conroy et al. 2013, and references therein). As the stellar metallicities reflects the gas-phase metallicities at the time of star formation, the combined measurements of stellar and gas-phase metallicities over cosmic time puts powerful constraints on galaxy formation models (Bresolin et al. 2009; Sommariva et al. 2012).

In this Letter we take a step in this direction by comparing the stellar oxygen abundances of massive galaxies in the local Universe to the gas-phase oxygen abundances of their putative progenitors at early times. This comparison should be relatively straightforward for massive galaxies, as they formed most of their stars at redshifts $z \gtrsim 2$ (Thomas et al. 2005; Conroy et al. 2013). Therefore, there should be a direct correspondence between the gas-phase metallicities of massive galaxies at $z \gtrsim 2$ and the stellar metallicities of their descendants at $z = 0$.

This project has recently become possible due to the CANDELS and 3D-*Hubble Space Telescope* (*HST*) datasets, which provide mass-limited samples with accurate redshifts, and to the advent of the MOSFIRE spectrograph on the Keck Telescope (McLean et al. 2012). Furthermore, accurate stellar abundances of individual elements have recently been derived from averaged spectra of Sloan Digital Sky Survey galaxies of different masses (Conroy et al. 2013).

In order to link progenitor galaxies with their descendants, we require that they have the same cumulative number density (van Dokkum et al. 2010; Patel et al. 2013; Leja et al. 2013). This comparison at a constant number density is preferable to comparison at constant stellar mass, as it explicitly takes the mass evolution of galaxies into account.

Throughout the Letter, we assume a Chabrier initial mass function (IMF; Chabrier 2003) and a ΛCDM cosmology with $H_0 = 70$ km s^{-1} Mpc^{-1}, $\Omega_M = 0.3$, and $\Omega_\Lambda = 0.7$.

2. SAMPLE SELECTION

We select spectroscopic targets in the UKIDSS-UDS field from version 2.1 of the 3D-*HST* survey catalogs (Brammer

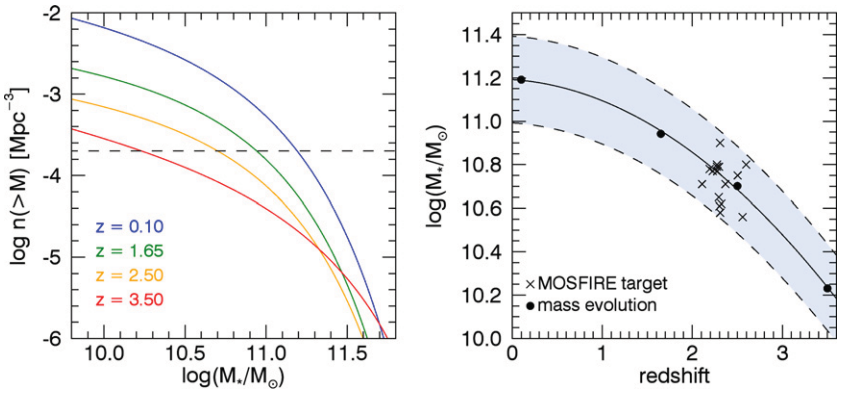

Figure 1. Stellar mass evolution is inferred at a constant cumulative number density of 2×10^{-4} Mpc^{-3} (dashed horizontal line) from the mass functions of Marchesini et al. (2009) (colored lines). The right panel shows the mass evolution at this number density (solid circles) and a quadratic parameterization (solid line, Equation (1)). The selection area (±0.2 dex) is shaded in light blue, and target galaxies are marked with crosses.

(A color version of this figure is available in the online journal.)

Table 1
Spectroscopic Targets

ID	α (J2000)	δ (J2000)	F140W	$\mathcal{R}^a$	$\log(M_*)$ ($M_\odot$)	SFR ($M_\odot$ yr^{-1})	r_e^b (kpc)	$z_{3D\text{-}HST}$	z_{spec}	[N II]/Hα
2522	34.42735	−5.26471	22.69	24.34	10.61	242	5.26	2.30	2.315	$0.29^{+0.03}_{-0.02}$
5698	34.44652	−5.24892	23.55	26.24	10.71	141	2.82	2.11	2.127	$0.31^{+0.03}_{-0.03}$
8461	34.42749	−5.23648	23.66	26.24	10.78	142	3.31	2.19	2.299	$0.28^{+0.03}_{-0.02}$
10746	34.39999	−5.22679	22.39	24.09	10.71	88.	6.31	2.37	2.541	$0.16^{+0.03}_{-0.03}$
19440	34.41029	−5.18816	23.27	25.17	10.77	30.	4.63	2.28	2.291	$0.28^{+0.02}_{-0.02}$
24828	34.42530	−5.16451	23.30	24.93	10.80	67.	5.90	2.27	2.243	$0.31^{+0.03}_{-0.03}$
3956	34.46006	−5.25758	23.50	26.57	10.79	0	1.46	2.27	···	···
5326	34.43100	−5.25042	26.08	27.54	10.56	1	3.19	2.56	···	···
9277	34.42780	−5.23286	24.41	26.77	10.80	0	1.61	2.60	···	···
10771	34.42257	−5.22659	23.55	25.21	10.65	21	3.73	2.29	···	···
11700	34.44719	−5.22188	24.57	26.82	10.77	9	2.71	2.23	···	···
11909	34.42215	−5.22073	23.88	27.18	10.75	0	0.63	2.50	···	···
12447	34.40580	−5.21886	22.79	25.95	10.79	1	0.86	2.30	···	···
16478	34.40424	−5.20082	24.33	27.35	10.62	0	3.97	2.32	···	···
18367	34.38511	−5.19237	23.60	27.07	10.58	0	0.76	2.31	···	···
22984	34.41577	−5.17188	23.81	26.42	10.90	269	2.44	2.31	···	···

Notes.
[a] $\mathcal{R}$-band magnitude, defined in Steidel & Hamilton (1992).
[b] Sizes calculated in the *H*-band as described in van der Wel et al. (2012).

et al. 2012). The 3D-*HST* catalogs contain redshifts and stellar masses derived from a combination of *HST*/G141 grism spectra and deep photometric data, with wavelength coverage from UV to *Spitzer*/IRAC as described in R. E. Skelton et al. (in preparation). Reported stellar masses are the current mass in stars and stellar remnants. When possible, the star formation rates (SFRs) are based on the UV+IR flux, with the IR determined from *Spitzer*/MIPS; otherwise, for fainter objects, they come from fits of stellar population synthesis models to the stellar spectral energy distributions (SEDs). As shown in Wuyts et al. (2011) the techniques give consistent answers where they overlap. We note that Hα emission in detected galaxies constitutes a median of 5% of the *K*-band flux, and thus has a negligible effect on broadband photometry. Catalog information and emission line properties for the targeted sample are shown in Table 1.

The targets are selected at a fixed cumulative number density of 2×10^{-4} Mpc^{-3} in the stellar mass functions of Marchesini et al. (2009), which are ∼100% complete in the relevant mass and redshift range. Selecting galaxies at a constant number density will effectively link galaxies across different redshifts if the stellar mass rank order of galaxies is approximately conserved with time, or alternatively, if processes that break rank order (i.e., merging or scatter in growth rates) have little effect on average galaxy properties. Leja et al. (2013) found this technique is effective in predicting the median descendant stellar mass from $z = 3$ to $z = 0$ to $\leqslant$0.15 dex in a semi-analytical model. This selection corresponds to a redshift-dependent stellar mass criterion, shown in Figure 1. The stellar mass evolution is parameterized as:

$$\log\left(\frac{M_*(z)}{M_\odot}\right) = 11.19 - 0.03z - 0.07z^2. \quad (1)$$

Specifically, we target galaxies that have stellar masses within ±0.2 dex of this relationship. We further require that Hα and [N II] fall both within the *K*-band filter and on the MOSFIRE detector, effectively creating a joint constraint on the redshift and the (α, δ) of each target. These selection criteria result in a mask with 16 galaxies, with redshifts $2.1 < z < 2.55$.

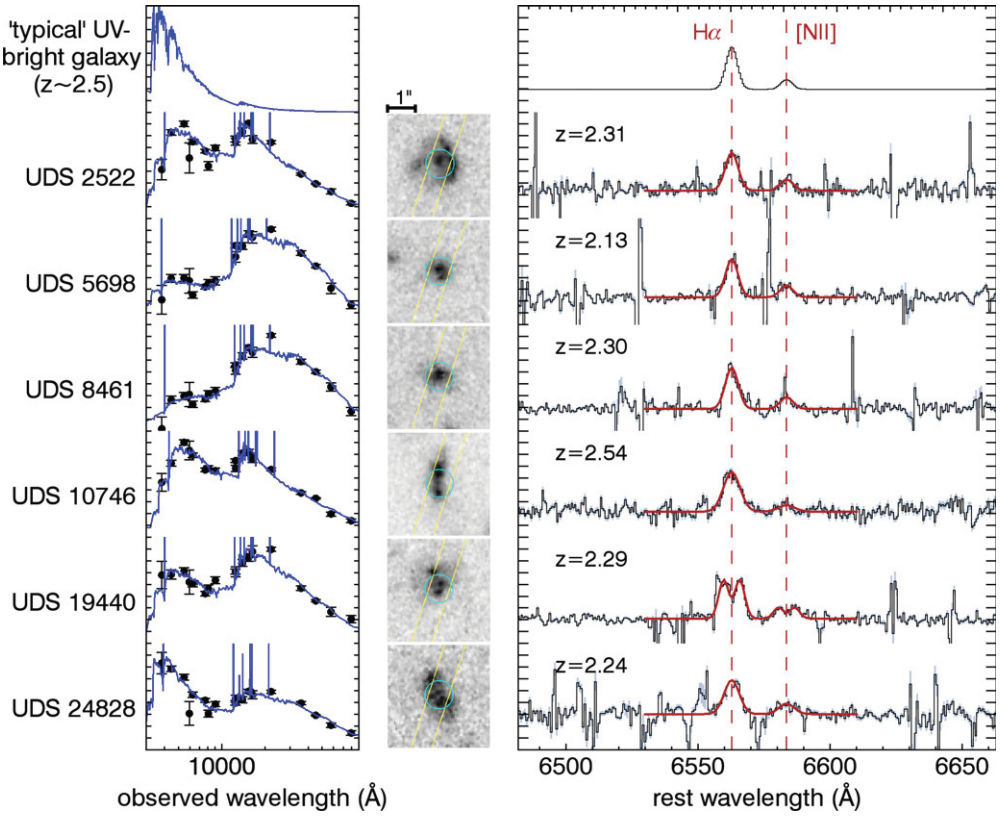

Figure 2. Template SEDs (blue) fit to the broadband photometry (black) are shown for each galaxy with detected emission lines. The units are arbitrarily normalized in f_λ. The center column has *HST*/F160W cutouts with the MOSFIRE slit orientation overlaid. The MOSFIRE *K*-band spectra are on the right, with 1σ errors in blue. Single Gaussian fits to the Hα and [N II] line profiles are overlaid in red. UDS-19440 is fit with a double Gaussian to account for the rotational line profile. We also include the SED of a typical UV-bright galaxy, constructed with the stellar population synthesis models of Bruzual & Charlot (2003) and typical UV-bright stellar population parameters from Papovich et al. (2001).

(A color version of this figure is available in the online journal.)

3. OBSERVATIONS AND DATA REDUCTION

The MOSFIRE *K*-band observations were conducted on 2013 January 20, with $\sim$1.″5 seeing. An ABAB dither pattern with a 1.″5 nod was used. Slit widths were 0.″7. A single mask was observed with 16 targets for 85 minutes, with six of the targets showing clear line emission. We estimate that sky lines obscure only $\sim$3% of the spectral range for emission lines with a central per-pixel signal-to noise ratio (S/N) = 20, typical for detected emission lines. The non-detections are thus likely caused by intrinsically weak or dust-obscured galaxy emission lines, rather than overlap of intrinsically bright lines with sky emission features.

The MOSFIRE data reduction pipeline[12] was used to reduce the spectroscopic data. The pipeline performs flat fielding, wavelength calibration, sky subtraction, and cosmic ray removal before producing a final two-dimensional output with an associated variance map. One-dimensional spectra were extracted using the optimal extraction method of Horne (1986). No flux calibration or reddening correction was necessary for this study.

The *K*-band spectra for targets with detected emission lines are shown in Figure 2, along with SEDs and F160W direct images. Hα and [N II] emission lines are fit with Gaussian profiles; the only exception is UDS-19440, which is fit with a double Gaussian to properly model the line profile. [N II] and Hα are fit simultaneously, with their line widths and redshifts constrained to the same value to improve accuracy when fitting the weaker [N II] line. The adopted fluxes are the areas of the Gaussians. Errors in the line profile are determined by perturbing each flux value within a Gaussian probability distribution, then remeasuring the line profile. The width of the Gaussian probability distribution is set to the 1σ flux error in the pixel. The errors on measured parameters are taken as the 68% range in derived parameters over 1000 iterations of perturbed spectra.

[12] https://code.google.com/p/mosfire/

4. RESULTS

4.1. [N II]/Hα Ratios

We measure a mean [N II]/Hα ratio of 0.27 ± 0.01 (error in the mean) $\pm$ 0.05 (standard deviation) in our sample.

We compare the relationship between stellar mass and [N II]/Hα in our sample and in UV-selected samples (Figure 3). By contrasting data rather than derived quantities, we cleanly assess potential differences in [N II]/Hα ratio between different samples.

Specifically, we compare our measurements to those of Erb et al. (2006a) and Kulas et al. (2013). These studies select spectroscopic targets to be bright in the rest-frame UV ($\mathcal{R} <$ 25.5) and to fulfill color–color criteria in the rest-frame UV, as described in Steidel et al. (2004) and Adelberger et al. (2004). The data from Erb et al. (2006a) are stacked spectra with $\sim$15 galaxies per point.

The stellar masses in Erb et al. (2006a) are reported as the integral of the SFR. In order to compare with our data, we convert the Erb et al. (2006a) stellar masses into the mass in

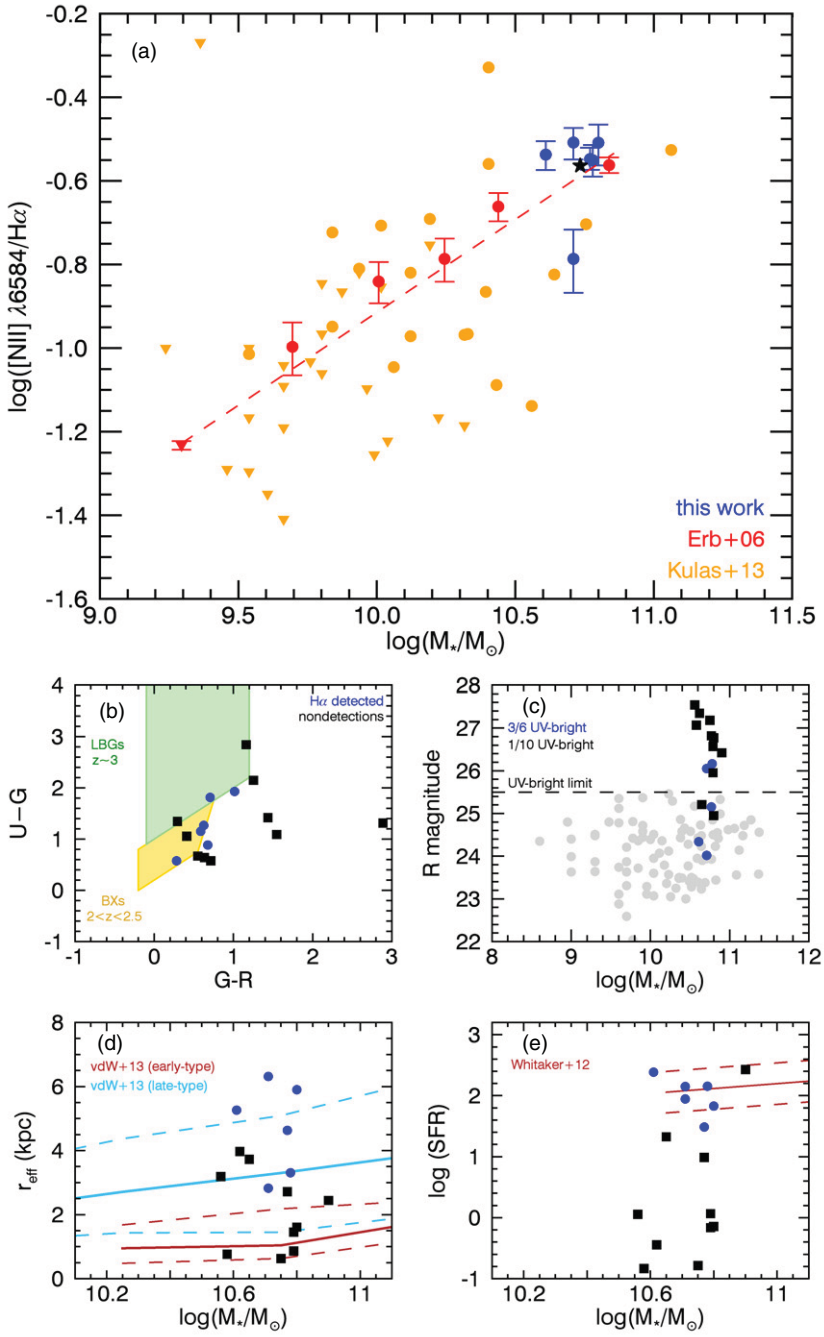

Figure 3. In all panels, blue circles are galaxies with detected emission lines, while black squares are non-detections. (a) Comparing [N II]/Hα ratios from our mass-selected sample (blue) to those from UV-selected samples (orange, red). The mean of our mass-selected sample is marked with a black star. Galaxies with upper limits on [N II]/Hα are marked with downward triangles. The Erb et al. (2006a) data are from composite spectra. The red dashed line is a linear fit to the Erb et al. (2006a) data. (b) The UV-bright color–color selection boxes are taken from Steidel et al. (2004). (c) Gray points are from the UV-bright sample of Erb et al. (2006b), and the UV-bright magnitude limit is indicated with a dashed line. (d) The size–mass relations are taken from Sérsic fits to the circularized H-band light profile at $z \sim 2.25$ (A. van der Wel, in preparation): median values are shown as solid lines, while the 16th and 84th percentiles are dashed lines. (e) The star forming sequence is taken from Whitaker et al. (2012) and marked with a solid red line, with 1σ scatter denoted by dashed lines.

(A color version of this figure is available in the online journal.)

stars and stellar remnants using the following formula:

$$\log\left(\frac{M}{M_{\rm Erb}}\right) = 1.06 - 0.24T + 0.01T^2, \qquad (2)$$

with $T \equiv \log(\text{age/yr})$, and ages taken from Erb et al. (2006a). The formula is a fit to the mass loss rates in the Bruzual & Charlot (2003) models for a Chabrier IMF, and applies only to ages >2 Myr.

Figure 3 shows that mass-selected galaxies have similar [N II]/Hα ratios compared to UV-selected galaxies. We quantify the significance of this result by simulating our observations using population statistics from the UV-selected samples. First, we fit a linear relationship to the Erb et al. (2006a) points, finding:

$$\log([\text{N ii}]/\text{H}\alpha) = -5.36 + 0.44\log(M_*/M_\odot). \qquad (3)$$

We use this relationship to estimate the UV-selected [N II]/Hα ratio at the average stellar mass of our sample: $\log(\langle M \rangle_*/M_\odot) = 10.73$. We calculate the biweight scatter (Beers et al. 1990) about the relationship to be 0.22 dex, using the Kulas et al. (2013) galaxies with $M_* > 10^{10}\ M_\odot$. We then simulate our observations by repeatedly sampling six galaxies from a Gaussian probability distribution with a mean and scatter fixed to the values above. This results in a mean [N II]/Hα ratio greater than our measured ratio only 40% of the time. This mass-selected sample thus does not have significantly higher [N II]/Hα ratios than UV-selected samples.

To further explore whether mass-selected, Hα-detected galaxies are different from UV-selected galaxies of the same mass, we include two panels in Figure 3 that explore what fraction of the mass-selected sample does not fulfill the selection criteria for a UV-bright sample. Our sample is split into galaxies with detected emission lines and non-detections. $\mathcal{U}$, $\mathcal{G}$, and $\mathcal{R}$ magnitudes are measured directly from the best-fit EAZY template (Brammer et al. 2008), then shown relative to the UV-bright selection criteria. The results indicate that 50% of the galaxies with detected emission lines fit the UV-bright selection criteria,[13] but only 10% of galaxies without detected emission lines fit the same criteria. The whole sample is thus primarily UV-faint: however, 50% of the galaxies with detected line emission are UV-bright.

4.2. Oxygen Abundances

We next convert the measured [N II]/Hα ratios into oxygen abundances. To demonstrate the spread in oxygen abundance between metallicity calibrations, we calculate the oxygen abundance in three different calibration systems: Maiolino et al. (2008; M08), Denicoló et al. (2002; D02), and Pettini & Pagel (2004; PP04).

The M08 relationship between observed [N II]/Hα ratio and oxygen abundance is:

$$\log([\mathrm{N\,II}]/\mathrm{H}\alpha) = c_0 + c_1 x + c_2 x^2 + c_3 x^3 + c_4 x^4, \quad (4)$$

with $c_0 = -0.7732$, $c_1 = 1.2357$, $c_2 = -0.2811$, $c_3 = -0.7201$, $c_4 = -0.333$, and $x \equiv 12 + \log(\mathrm{O/H}) - 8.69$. The scatter in this conversion is taken to be 0.1 dex.

We find a mean oxygen abundance of $12 + \log(\mathrm{O/H}) = 8.87 \pm 0.04$, 8.70 ± 0.10 and 8.57 ± 0.08 for the M08, D02, and PP04 calibrations respectively. The quoted error is the error in the mean, while the standard deviations are 0.09, 0.08, and 0.08, again respectively. These mean abundances range from 0.12 dex below the solar value of $12 + \log(\mathrm{O/H}) = 8.69$ (Asplund et al. 2009) for the PP04 calibration to 0.18 dex above solar for M08.

4.3. Comparison to Stellar Abundances at $z = 0$

We now compare the gas-phase oxygen abundances to the stellar oxygen abundances of nearby galaxies. We adopt the stellar oxygen abundances measured in Conroy et al. (2013). This study analyzes spectra from the inner 0.4–0.8 effective radii of local quiescent galaxies stacked in bins of stellar velocity dispersion, and fits a full-spectrum model to them, described in Conroy & van Dokkum (2012). The model constrains the abundances of individual elements, including oxygen. To compare with our results, we derive the average stellar mass for these stacks, and interpolate the stellar oxygen abundance at the expected descendant mass. Specifically, we interpolate between the two bins with $\log(\sigma/\mathrm{km\ s^{-1}}) = 2.39$ and 2.47, with corresponding stellar masses of 10.96 and 11.34. This results in an oxygen abundance of $12 + \log(\mathrm{O/H}) = 8.95^{+0.03}_{-0.03}$. The error bars represent the stellar oxygen abundances as inferred at the edge of the mass selection box (see Figure 1).

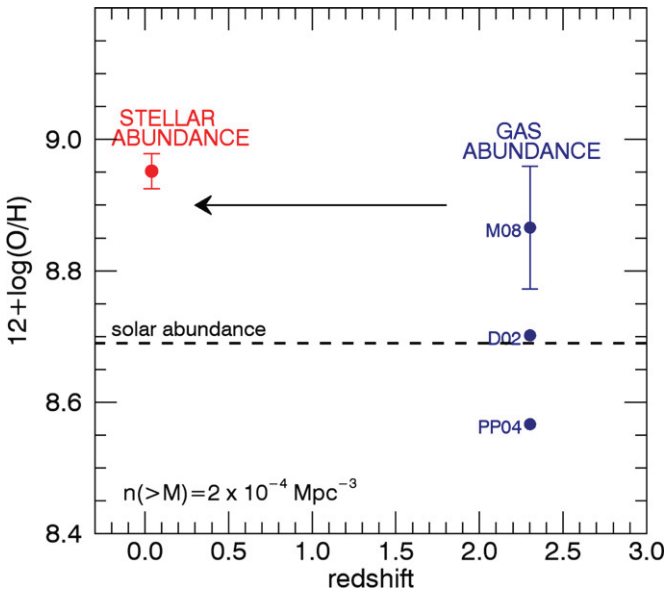

Figure 4. Comparing the gas-phase oxygen abundances of galaxies at $z \sim 2.3$ to the stellar abundances of local quiescent galaxies at the same number density. The mean gas-phase metallicities from multiple metallicity calibrations are shown in dark blue. The scatter in these calibrations is ∼0.1–0.2 dex. The solar abundance is from Asplund et al. (2009). The gas-phase error bar is the standard deviation of the metallicities; it is only shown for the M08 calibration for clarity. (A color version of this figure is available in the online journal.)

We can now compare these $z = 0$ stellar abundances to the high-redshift gas-phase metallicities derived in Section 4.2. If the high-redshift galaxies are progenitors of the low-redshift galaxies, and we are observing the main epoch of star formation in the high-redshift galaxies, then the high-redshift gas-phase abundance should match the low-redshift stellar metallicity. Interestingly, the gas-phase metallicities are lower than the stellar abundances, with the difference depending on the calibration method. PP04 produces the largest inconsistency, with the stellar abundance nearly 0.4 dex higher than the gas metallicity. The best match comes from the M08 calibration, which produces gas metallicities that are only 0.08 dex lower than the stellar abundance.

5. DISCUSSION

In this Letter, we have measured [N II]/Hα ratios from Keck/MOSFIRE *K*-band spectroscopy of a mass-selected sample at high redshift. We demonstrate that these [N II]/Hα ratios are similar to those measured in surveys of UV-bright galaxies. We measure an average [N II]/Hα ratio of 0.27, corresponding to an average gas-phase oxygen abundance of $12+\log(\mathrm{O/H}) = 8.57$–$8.87$, depending on the metallicity calibration adopted. Taking Figure 4 at face value, we would conclude that the M08 calibration gives the best match to the $z = 0$ stellar abundances, and should therefore be preferred over the other calibrations. However, there are many sources of systematic uncertainty in this study.

We first consider the sources of the differences in the three calibrations. The M08 oxygen abundance is calculated from a

[13] If we instead ask whether these galaxies would be considered UV-bright when placed at *any* redshift, this changes to 67%.

combination of the direct T_e method for galaxies with log(O/H) + 12 < 8.35, and with strong line ratios and the photoionization models of Kewley & Dopita (2002) for log(O/H) + 12 > 8.35. D02 derives oxygen abundances primarily from the direct T_e method, with roughly one third of their abundances from oxygen or sulfur strong line ratios. PP04 uses 97% direct T_e abundances. All three studies then derive a relationship between [N II]/Hα ratio and oxygen abundance.

The spread in metallicity calibrations may be related to issues with the photoionization models, or temperature gradients and fluctuations that cause metallicities determined by the direct T_e method to be underestimated (Peimbert 1967; Kewley & Ellison 2008). Observational studies of optical recombination lines show a systematic differences of 0.26 ± 0.09 dex with the T_e method (Esteban et al. 2009), which may explain some of the variation.

There is also emerging evidence that, at high redshift, metallicities based on [N II]/Hα are offset from those based on [O II]λ3727, [O III]λ4959, 5007 and Hβ, even within the same system of metallicity calibrations (Newman et al. 2013; Cullen et al. 2013). Specifically, metallicities based on oxygen lines are $\sim$0.3 dex lower than those based on nitrogen lines. This difference is attributed to different physical conditions in star forming regions at high redshift, and it is unclear which calibrations, if either, represents the "true" gas-phase metallicity.

Another uncertainty in our study stems from the fact that, in addition to metallicity, [N II] flux is sensitive to the presence of both an active galactic nucleus (AGN) and shock excitation. It is unfortunately not possible to separate out the AGN contribution to the [N II] flux without high-resolution integral field unit (IFU) data (Förster Schreiber et al. 2011). However, all detected galaxies in our sample have log([N II]/Hα) < -0.5; the theoretical high-redshift Baldwin, Phillips, & Terlevich diagram indicates that significant AGN contribution in this regime is unlikely (Kewley et al. 2013), though it may exist at a low level.

We note that the presence of radiative shocks, AGN, and/or different physical conditions at high redshift would imply *lower* oxygen abundances than indicated by the measured [N II]/Hα ratios.

It may also be that the stellar oxygen abundances are overestimated. The measurement of oxygen abundance in old unresolved stellar populations is notoriously difficult (see Conroy 2013 and references therein). In the Conroy & van Dokkum (2012) spectral model, the oxygen abundance is primarily derived from a combination of TiO lines and molecular equilibrium involving CNO. The trend [O/Fe]$\sim$[Mg/Fe] matches that as measured in the Milky Way (Edvardsson et al. 1993, though see also Bensby et al. 2013), suggesting that the stellar oxygen abundance measurements are robust.

We also consider the possibility of misidentification of the descendant galaxies. The predicted stellar mass evolution from $z \sim 2.3$ to $z = 0$ for these galaxies is +0.4 dex. If instead the stellar mass evolution were +0.1/+0.7 dex, this results in negligible change of -0.05/+0.05 dex in the oxygen abundance of their descendants. This is due to the flat relationship between the stellar mass and stellar metallicity (Panter et al. 2008). This comparison is thus robust against errors in descendant matching. Additionally, the stellar mass growth at this number density is primarily not through additional star formation, but rather accretion (van Dokkum et al. 2010; Patel et al. 2013). These accreted galaxies presumably had lower metallicities than the main progenitor galaxy, which means that they would lower the total luminosity-weighted stellar metallicity (Greene et al. 2013). Taking this process into account would therefore, if anything, increase the discrepancy in Figure 4.

Perhaps the most likely possibility is that selection by stellar mass may still be biased, in the sense that the most metal-rich galaxies do not have detectable emission lines. Only 37.5% of our sample has detected emission lines; furthermore, the galaxies without detected emission lines are not a random subset of the sample. The last two panels in Figure 3 examine the different properties of detections and non-detections in our sample. Galaxies with detected emission lines consistently have larger effective radii and higher SFRs than galaxies without detected emission lines.

These properties are known to correlate with the gas-phase metallicity of the galaxies. For example, observations suggest that gas-phase metallicity and SFR are anticorrelated (Mannucci et al. 2010). Furthermore, gas-phase metallicity varies by up to 0.2 dex at fixed stellar mass as a function of half-light radius, with larger galaxies having lower metallicities (Tremonti et al. 2004; Ellison et al. 2008).

Even in galaxies with detected emission lines, some unknown fraction of the star formation may be obscured by dust. Perhaps the detected line flux originates from "shells" or "rings" of Hα, as seen in IFU studies (Förster Schreiber et al. 2011), while the star forming core remains heavily obscured. UDS-22984 may host such obscured star formation: it has a 24 μm flux indicating a SFR of $\sim$270 $M_\odot$ yr^{-1} and an SED-estimated $A_V = 2.6$, yet no detected line emission. Since dust correlates with metallicity, this galaxy will likely be more oxygen-rich than galaxies with unobscured star formation. If such heavily obscured star formation is common at high redshift, it remains a possibility that the star forming progenitors of local ellipticals have yet to be detected.

We thank the anonymous referee for an outstanding report which substantially improved the Letter. Support from *HST* grant GO-12177 is gratefully acknowledged. Some of the data presented herein were obtained at the W.M. Keck Observatory, which is operated as a scientific partnership among the California Institute of Technology, the University of California and the National Aeronautics and Space Administration. The Observatory was made possible by the generous financial support of the W.M. Keck Foundation.

REFERENCES

Adelberger, K. L., Steidel, C. C., Shapley, A. E., et al. 2004, ApJ, 607, 226
Asplund, M., Grevesse, N., Sauval, A. J., & Scott, P. 2009, ARA&A, 47, 481
Beers, T. C., Flynn, K., & Gebhardt, K. 1990, AJ, 100, 32
Bensby, T., Feltzing, S., & Oey, M. S. 2013, arXiv:1309.2631
Brammer, G. B., van Dokkum, P. G., & Coppi, P. 2008, ApJ, 686, 1503
Brammer, G. B., van Dokkum, P. G., Franx, M., et al. 2012, ApJS, 200, 13
Bresolin, F., Gieren, W., Kudritzki, R.-P., et al. 2009, ApJ, 700, 309
Bruzual, G., & Charlot, S. 2003, MNRAS, 344, 1000
Chabrier, G. 2003, PASP, 115, 763
Conroy, C. 2013, ARA&A, 51, 393
Conroy, C., Graves, G., & van Dokkum, P. 2013, arXiv:1303.6629
Conroy, C., & van Dokkum, P. 2012, ApJ, 747, 69
Cullen, F., Cirasuolo, M., McLure, R. J., & Dunlop, J. S. 2013, arXiv:1310.0816
Davé, R., Finlator, K., & Oppenheimer, B. D. 2012, MNRAS, 421, 98
Denicoló, G., Terlevich, R., & Terlevich, E. 2002, MNRAS, 330, 69
Edvardsson, B., Andersen, J., Gustafsson, B., et al. 1993, A&A, 275, 101
Ellison, S. L., Patton, D. R., Simard, L., & McConnachie, A. W. 2008, ApJL, 672, L107
Erb, D. K., Shapley, A. E., Pettini, M., et al. 2006a, ApJ, 644, 813
Erb, D. K., Steidel, C. C., Shapley, A. E., et al. 2006b, ApJ, 646, 107
Esteban, C., Bresolin, F., Peimbert, M., et al. 2009, ApJ, 700, 654
Förster Schreiber, N. M., Shapley, A. E., Erb, D. K., et al. 2011, ApJ, 731, 65

Gallazzi, A., Charlot, S., Brinchmann, J., White, S. D. M., & Tremonti, C. A. 2005, MNRAS, 362, 41
Greene, J. E., Murphy, J. D., Graves, G. J., et al. 2013, ApJ, 776, 64
Horne, K. 1986, PASP, 98, 609
Kewley, L. J., & Dopita, M. A. 2002, ApJS, 142, 35
Kewley, L. J., & Ellison, S. L. 2008, ApJ, 681, 1183
Kewley, L. J., Maier, C., Yabe, K., et al. 2013, arXiv:1307.0514
Kulas, K. R., McLean, I. S., Shapley, A. E., et al. 2013, ApJ, 774, 130
Leja, J., van Dokkum, P., & Franx, M. 2013, ApJ, 766, 33
Maiolino, R., Nagao, T., Grazian, A., et al. 2008, A&A, 488, 463
Mannucci, F., Cresci, G., Maiolino, R., Marconi, A., & Gnerucci, A. 2010, MNRAS, 408, 2115
Marchesini, D., van Dokkum, P. G., Förster Schreiber, N. M., et al. 2009, ApJ, 701, 1765
McLean, I. S., Steidel, C. C., Epps, H. W., et al. 2012, Proc. SPIE, 8446, 84460J
Newman, S. F., Buschkamp, P., Genzel, R., et al. 2013, arXiv:1306.6676
Panter, B., Jimenez, R., Heavens, A. F., & Charlot, S. 2008, MNRAS, 391, 1117
Papovich, C., Dickinson, M., & Ferguson, H. C. 2001, ApJ, 559, 620
Patel, S. G., van Dokkum, P. G., Franx, M., et al. 2013, ApJ, 766, 15
Peimbert, M. 1967, ApJ, 150, 825
Pettini, M., & Pagel, B. E. J. 2004, MNRAS, 348, L59
Sommariva, V., Mannucci, F., Cresci, G., et al. 2012, A&A, 539, A136
Steidel, C. C., & Hamilton, D. 1992, AJ, 104, 941
Steidel, C. C., Shapley, A. E., Pettini, M., et al. 2004, ApJ, 604, 534
Stott, J. P., Sobral, D., Bower, R., et al. 2013, MNRAS, in press
Thomas, D., Maraston, C., Bender, R., & Mendes de Oliveira, C. 2005, ApJ, 621, 673
Tremonti, C. A., Heckman, T. M., Kauffmann, G., et al. 2004, ApJ, 613, 898
van der Wel, A., Bell, E. F., Häussler, B., et al. 2012, ApJS, 203, 24
van Dokkum, P. G., Whitaker, K. E., Brammer, G., et al. 2010, ApJ, 709, 1018
Whitaker, K. E., van Dokkum, P. G., Brammer, G., & Franx, M. 2012, ApJL, 754, L29
Wuyts, S., Förster Schreiber, N. M., van der Wel, A., et al. 2011, ApJ, 742, 96
Zahid, H. J., Geller, M. J., Kewley, L. J., et al. 2013, ApJL, 771, L19